Creation of Large Temperature Anisotropies in a Laboratory Plasma

C.B. Beatty,[1] T.E. Steinberger,[1] E. Aguirre,[2] R.A. Beatty,[1] K. Klein,[3] J.W. McLaughlin,[1,4] L. Neal,[1] and E.E. Scime[1]

[1)] *Department of Physics and Astronomy, West Virginia University, Morgantown, WV 26506*[a)]

[2)] *Department of Physics, Auburn University, Auburn, AL 36849*

[3)] *Department of Planetary Sciences, University of Arizona, 85721*

[4)] *Department of Physics and Astronomy, University of Iowa, Iowa City, IA 52242*

(Dated: October 30, 2020)

Ion temperature anisotropy in an expanding magnetized plasma is investigated using laser induced fluorescence (LIF). Parallel and perpendicular ion velocity distribution functions (IVDFs) were measured simultaneously with high spatial resolution in the expanding plasma. Large ion temperature anisotropies ($T_{\perp\, i}/T_{\|\, i} \sim 10$) are observed in a conical region at the periphery of the expanding plasma plume. A simple 2D Boris Stepper model that incorporates the measured electric field structure is able to reproduce the gross features of the measured perpendicular IVDFs. A Nyquist stability analysis of the measured IVDFs suggests that multiple instabilities with $k_\perp \rho_i \sim 1$ and $k_{||}\rho_i \sim 0.2$ are likely to be excited in these plasmas.

I. INTRODUCTION

Laboratory and space measurements of velocity space distributions of ions and electrons exhibit quasi-isotropicity, even under conditions for which large thermal anisotropy is expected. For example, standard models of the radially expanding solar wind predict significant thermal anisotropy (the ratio of temperature perpendicular and parallel to the local magnetic field) as a result of conservation of adiabatic moments.[1] Yet, measurements provide strong evidence that the ion thermal anisotropy ($T_{\perp\, i}/T_{\|\, i}$) in the solar wind is constrained by instability thresholds that are functions of the ion thermal anisotropy and the ratio of thermal to magnetic pressures, $\beta_{\|\, i} = 8\pi n_i k_B T_{\|\, i}/B^2$.[2–4] Electrons in the solar wind exhibit much smaller levels of thermal anisotropy than ions for nearly all solar wind conditions, yet the electron thermal anisotropy also appears to be constrained.[5] Solar wind ion thermal anisotropies near 1 AU as measured by the Wind spacecraft are shown in Fig. 1 as a function of parallel β and ($T_{\perp\, i}/T_{\|\, i}$).[6] Note that in the weakly collisional plasma of the solar wind, ion thermal anisotropies range from 0.2 to 3, peaking at values of $\beta \sim 0.3$. In the context of the solar wind at 1 AU, an ion temperature anisotropy of 3 is large. While Helios observations do show a decrease in the solar wind ion thermal anisotropy from 0.3 to 1 AU, the decrease in anisotropy is inconsistent with expectations for adiabatic processes, i.e., additional heating and anisotropy limiting processes also appear to constrain the ion thermal anisotropy in the inner heliosphere.[1]

The features of widespread interest in the solar wind data shown in Fig. 1 are the curves bounding the ion (proton) temperature anisotropies. The curves are defined by the expression ($T_{\perp\, i}/T_{\|\, i} = 1+S(\beta_{\|\, i}-\beta_{\|\, 0})^{-a}$), where S, $\beta_{\|\, 0}$, and a are empirical fitting parameters obtained from solutions of linear dispersion relations for instabilities driven by bi-Maxwellian proton velocity distributions.[7–9] If it is possible to craft a universal expression relating ($T_{\perp\, i}/T_{\|\, i}$) to β, partial closure of the Vlasov equations (specifically the energy equation) could be effected for a wide variety of physical systems - even for those in which the mean free path of the particles is large compared to the system size (the limit in which standard Chapman-Enskog asymptotic closure techniques fail). While the bounding of the measurements is likely explained by instability thresholds and Alfvén-cyclotron resonant heating effects (which constrain the left side of the plots in Fig. 1),[10,11] the fact that so many of the measurements are nearly isotropic is itself a remarkable characteristic of the solar wind.[12] To explain the dominance of isotropic distributions in solar wind measurements, Verscharen et al. have proposed that large-scale compressive fluctuations continually drive the collisionless solar wind towards instability thresholds until any anisotropy is eliminated.[13]

The same instabilities that are predicted to constrain the anisotropy in the solar wind appear are also believed to play important roles in the terrestrial magnetosheath, a near-Earth region of space consisting primarily of shocked solar wind plasma. Studies in the 1990s found that the maximum ion thermal anisotropies in the magnetosheath lay below a threshold value that depends strongly on the plasma β.[14] The two instabilities most likely to grow in the high thermal pressure, $\beta \sim 1$, anisotropic conditions of the magnetosheath are the mirror mode, and the Alfvén Ion Cyclotron Instability (also known as the anisotropic ion cyclotron instability).[15–17] More recent studies have confirmed that the bounds on the ion thermal anisotropy in the magnetosheath share a great many characteristics with the solar wind measurements.[18] The theoretical models of the solar wind and the magnetosheath that generate instability threshold predictions such as those shown in Fig. 1 treat the protons as a single anisotropic distribution. For resonant instabilities, the velocity derivative

[a)] Electronic mail: cbb0017@mix.wvu.edu

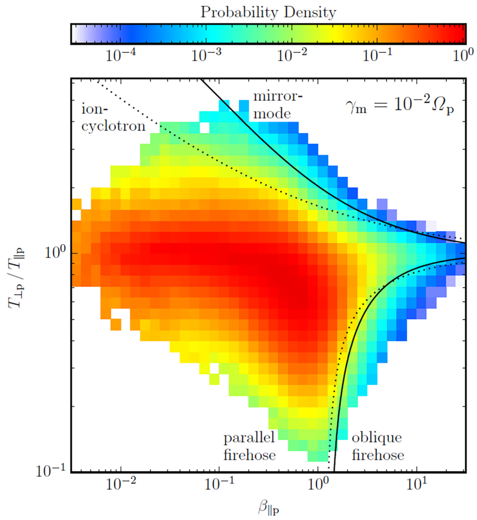

Figure 1. Probability distribution of the pristine solar wind in the β - $(T_{\perp\ i}/T_{\|\ i})$ plane. The instability thresholds for the four instabilities associated with proton temperature anisotropy are plotted for comparison. A signicant fraction of the distribution exceeds the two resonant thresholds (ion-cyclotron and parallel rehose), while the non-resonant mirror-mode and oblique-rehose thresholds set more precise boundaries to the data distribution. Adapted with permission from Figure 21 of Living Rev. Solar Phys. 16, 5621 (2019). Copyright 2019 Springer.

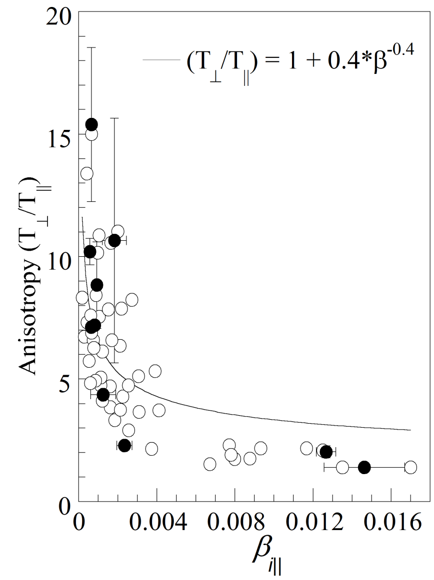

Figure 2. Ion temperature anisotropy versus β (open circles) in the LEIA facility. These data were obtained over a wide range of operating magnetic fields but at fixed rf power and neutral pressure. Also shown are averaged values of anisotropy and β for nearly identical plasma conditions (solid circles) obtained on different days with standard deviation error bars.[3] Reprinted with permission from Phys. Plasmas 7, 2157 (2000). Copyright 2000 AIP Publishing LLC

of the distribution function, $f(v)$, at the resonant speed of the wave depends strongly on the details of the distribution function. Therefore, detailed measurements of $f(v)$ are critically important to understanding which instability mechanisms are likely to be active.

Laboratory studies of ion thermal anisotropy limits in the 1990s included detailed $f(v)$ measurements along with electrostatic and electromagnetic wave measurements. Keiter et al.[3,19] observed a β-dependent limit on ion thermal anistropy that was consistent with the predictions of Alfvén ion cyclotron instability thresholds (see Fig. 2). In those experiments, ion thermal anisotropies greater than 10 were observed along with enhanced electromagnetic fluctuations for the same operation conditions that resulted in the large values of $T_{\perp\ i}/T_{\|\ i}$. A significant challenge in those experiments was routinely creating ion distributions with values of of $T_{\perp\ i}/T_{\|\ i} > 5$.

Here we report a series of experiments in which large levels of ion thermal anisotropy ($T_{\perp\ i}/T_{\|\ i} > 5$) are routinely created in a spatially restricted region in an expanding laboratory plasma as a result of perpendicular ion energization in highly structured electric fields.[20] The long-term objective of these experiments to provide a testbed for studies of ion thermal anisotropy limits over a wide range of plasma conditions. For consistency with space-based measurements, the second moments of the measured parallel and perpendicular ion velocity distribution functions (IVDFs) are used to determine the effective parallel and perpendicular ion temperatures in the laboratory experiments. A simple Boris stepper model of the ion motion in the electrical field structure confirms that the observed significant perpendicular ion temperatures likely result from stochastic motion in the electric fields. Therefore, the measured anisotropies are not "classical" in the sense that the perpendicular and parallel velocity distributions are not simple Maxwellians - just with different temperatures. Instability analysis employing the measured ion velocity distributions confirms that ion beam instabilities are likely to be excited in these plasmas.

II. EXPERIMENTAL APPARATUS

The cylindrically symmetric LEIA (the Large Experiment on Instabilities and Anisotropies) facility (see Fig. 3) consists of a 0.1 m diameter, 0.72 m long Pyrex®source chamber mounted on a 0.15 m diameter, 0.9 m long stainless steel diagnostic chamber that opens up into a 2 m diameter, 4.5 m long expansion chamber. Up to 2.0 kW of rf power is coupled through a 19 cm long, $m = 1$ helical antenna over a frequency range of $6 - 18$ MHz. Ten water cooled electromagnets produce a steady-state, nearly uniform axial magnetic field of $0 - 1200$ G in the source. Seven water cooled

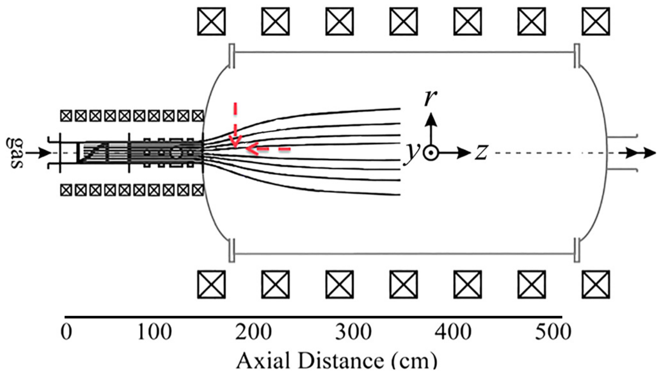

Figure 3. The magnetic field geometry (contours of constant magnetic flux) as the plasma expands from the plasma source into the expansion chamber. The *in-situ* probe accesses the expansion region downstream of the plasma source (identified by the red arrows).

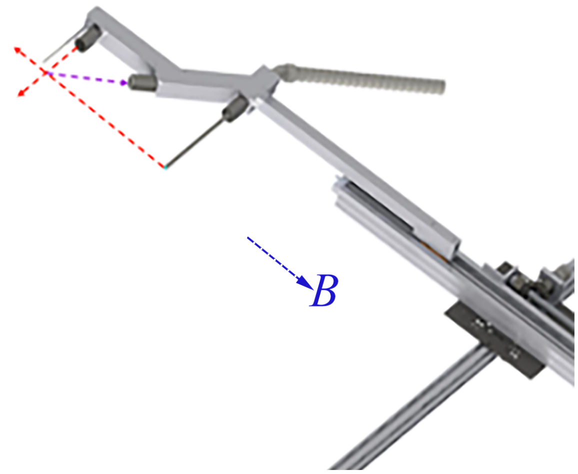

Figure 4. Schematic of the *in-situ* combined LIF and Langmuir probe. The two LIF injection paths are indicated with red dotted lines. Both the parallel and the perpendicular injections use the same collection path, shown in purple. The Langmuire probe tip projects from the 6.4 mm tube mounted at the end of the probe. The translation stage allows movement in the plane of the probe in both $\hat{z}$ and $\hat{r}$ directions with sub-mm resolution. The magnetic field direction is shown in blue.

electromagnets produce a steady-state, uniform axial magnetic field of $0 - 150$ G in the expansion chamber. Three turbo molecular drag pumps, one located at the end of the source and two at the end of the expansion chamber, maintain a base pressure of 10^{-7} Torr. The large pumping rate at the end of the expansion chamber (3200 l/s) results in a hollow neutral pressure radial profile[21] and a downstream pressure ten times smaller than the neutral pressure in the source during plasma source operation. Complete details of the LEIA facility are available elsewhere.[20,22,23]

For these experiments, the neutral fill pressure of argon is 0.17 mTorr. This fill pressure corresponds to an operating pressure of ~ 0.90 mTorr in the source and a pressure ≤ 0.1 mTorr in the expansion chamber. At these neutral pressures, the ion-neutral charge exchange collisional mean free path is tens of centimeters in the expansion chamber. These low pressure plasmas are destructive to the Pyrex®tube and careful impedance matching is required to minimize the amount of reflected power and the voltages on the rf antenna. The axial magnetic field in the source is 860 G and the expansion chamber magnetic field is 108 G. A magnetic field expansion ratio $B_{\mathrm{up}}/B_{\mathrm{down}} \sim 8$ is sufficient to induce spontaneous formation of an ion beam (~ 10 km/s) along the LEIA axis.[24]

The argon IVDFs in the $\hat{r}$ and $\hat{z}$ directions, relative to the LEIA axis, were measured with laser induced fluorescence (LIF). The Ar-II population is interrogated with a Sirah Matisse DR ring-dye laser pumped by a Spectra-Physics Millenia Pro laser. Approximately 1 W of 611.6616 nm light is produced from the dye laser. Upon exiting the dye laser, a small fraction ($\lesssim 5\%$) is split to a neutral iodine reference cell and a Bristol 621 wavelength meter. The remaining laser light is passed through an optical diode and a 50/50 beamsplitter. The two beams are passed through separate mechanical choppers before being coupled into a pair of 200 μm $\varnothing$ multimode optical fibers. The mechanical choppers are operated at unique frequencies that are carefully chosen to avoid common harmonic features. For this work, the chopper frequencies were 5 kHz and 2.7 kHz. The LIF scheme consists of excitation to the $4p^2F_{7/2}$ state which then decays to the $4s^2D_{5/2}$ state through emission of a single photon at 461.086 nm. Doppler broadening of the transition is the dominant line broadening mechanism. Zeeman splitting of the absorption line into π and σ transitions contributes insignificantly to the measured broadening for magnetic fields of ~ 100 G and ion temperatures > 0.1 eV.[25]

The two multimode optical fibers are coupled into the vacuum chamber through a dual-fiber feedthrough that then directs the separate beams into an *in-situ* scanning mechanical probe (Fig. 4). Argon IVDFs are simultaneously interrogated in the radial $\hat{r}$ and axial $\hat{z}$ directions with focused beams emanating from two optical paths. Fluorescent emission from both injections directions is collected from a separate viewing direction and coupled into a single 1 mm core optical fiber. The collected light passes through a 1 nm wide filter centered on the emission wavelength. The filtered light is then coupled into a Hammatsu photo-multiplier tube (PMT). The PMT signal is divided in half and sent to two Stanford Systems SR830 DSP lock-in amplifiers. Each lock-in amplifier is referenced to one of two mechanical choppers to differentiate the LIF signal from the spontaneous emission. The frequency of the laser is scanned 25 GHz over 150 s for a lock-in signal integration of 1 s or over 450 s for an integration time of 3s. This apparatus enables the simultaneous measurement of IVDFs in two directions at a single, highly-resolved,

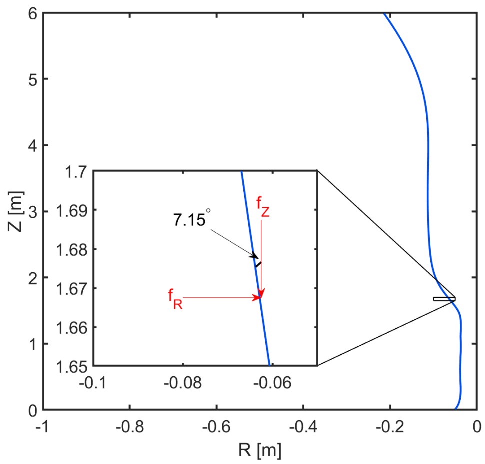

Figure 5. The magnetic field geometry in the measurement region. The magnetic field direction (blue line) is obtained from a three-dimensional model of the magnetic geometry that has been validated with direct measurements of the magnetic field.[23] The inset figure shows the angle of the magnetic field relative to the measurement directions in the measurement region.

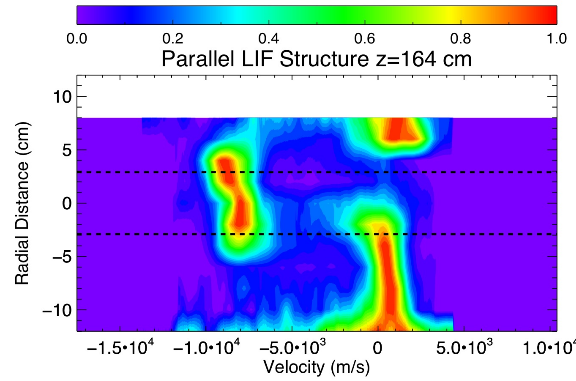

Figure 6. LIF measurements of the parallel ivdf as a function of radial position in the expansion region of LEIA (z = 164 cm). The intensities are normalized to unity at each measurement location to accentuate the changing spread of ion velocities with increasing radial position and plotted on a linear scale. Measurements were performed with a radial resolution of 1 cm and the image has been smoothed. Negative radial position values correspond to the side of the axis of the cylindrically symmetric system. Reprinted with permission from Phys. Plasmas 24, 123510 (2017). Copyright 2017 AIP Publishing

spatial location.

For a more detailed description of the *in-situ* scanning mechanical probe, we direct the readers to Refs.[20] and[26]. In addition to the LIF measurement capability, the probe also provides measurements of the local plasma potential, electron temperature, and ion density through an rf-compensated Langmuir probe. The 1 m long probe translates radially and axially to perform measurements with sub-mm resolution of the expanding plasma in a two-dimensional plane. For the high spatial resolution measurements reported here, the probe was scanned through a two-dimensional region bounded by -10 cm $< r < -5$ cm and 165 cm $< z <$ 169.8 cm. In this region, the magnetic field direction is at an angle of approximately 7° relative to the axis of the chamber (see Fig. 5). While it is unusual to use a coordinate system that allows for negative values of r, we have retained this nomenclature to emphasize the cylindrical nature of the experiment throughout all the discussions.

The large values of ($T_{\perp\ i}/T_{\parallel\ i} \sim 10$) are created in the plume of the expanding helicon source that supplies the plasma for LEIA. Experiments over the last decade have established the operating conditions necessary to trigger the spontaneous formation of a parallel ion beam, $v \sim 10$ km/s, in a variety of different helicon sources around the world.[23,27–31] Shown in Fig. 6 is a LIF measurement of the parallel ivdf as a function of radial location at z = 164 cm. In the inner region of the plasma column ($r <$ 5 cm), the entire parallel ivdf consists of a 8 km/s beam. Outside of this region, the parallel ivdf is at rest in the lab frame and the ion beam vanishes. Our previous measurements indicate that electrons under the rf antenna in the plasma source are heated and then free stream out of the plasma along the magnetic field, forming an annulus of energetic electrons in the expansion region.[20] The ambipolar field created by the electron loss pulls ions downstream in the center of the plasma, thereby creating the spatially localized ion beam. Subsequent measurements by other researchers have confirmed the essential features of this paradigm, i.e., the existence of a population of energetic electrons restricted to the periphery of the plasma column and an ion beam restricted to the center of the plasma column.[32–34]

In LEIA,[23] concurrent with the formation of the ion beam is the appearance of a concave, magnetic-field aligned, three-dimensional potential structure in the region of the strongest magnetic field gradient.[20,35] Along the periphery of the potential structure, significant perpendicular ion heating is observed.[20] An example of the perpendicular IVDF as a function of radial position (in 1 cm steps) at a single axial location in LEIA is shown in Fig. 7. The width in velocity space of the IVDF (the effective perpendicular temperature) clearly increases with radial position. In these measurements at moderate spatial resolution, the effective perpendicular ion temperature increases from much less than 1 eV at r = 0 cm to a few eV by r = 10 cm. It is these regions of enhanced effective perpendicular ion temperature that are the focus of the high spatial resolution measurements reported here. The reader may notice that the IVDF

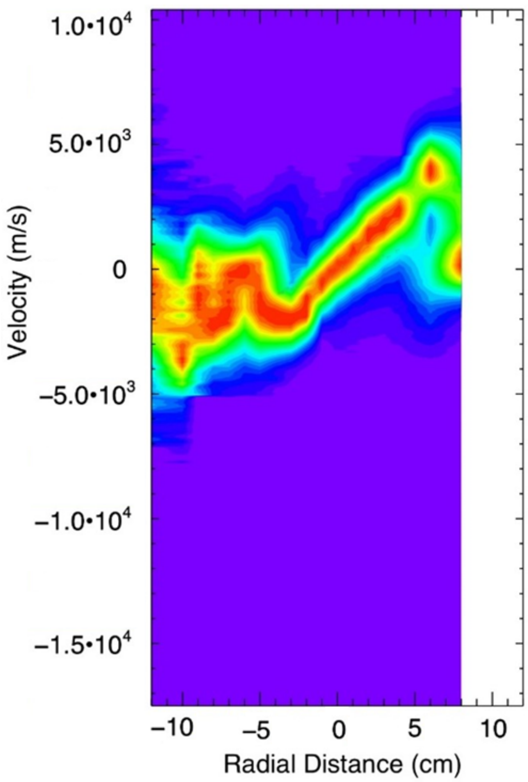

Figure 7. LIF measurements of the perpendicular ivdf as a function of radial position in the expansion region of LEIA (z = 164 cm). The intensities are normalized to unity at each measurement location to accentuate the changing spread of ion velocities with increasing radial position and plotted on a linear scale. Measurements were performed with a radial resolution of 1 cm and the image has been smoothed. Negative radial position values correspond to the side of the axis of the cylindrically symmetric system.

measurements in 7 are not completely symmetric. To reach the positive side of the chamber axis, the probe must pass through the core of the plasma, creating a significant perturbation of the plasma column.

III. ANISOTROPY MEASUREMENTS

Example LIF measurements of parallel and perpendicular IVDFs are shown in Fig. 8 for two different axial and radial locations in LEIA. At both locations the parallel IVDF is much narrower than the perpendicular IVDF. The perpendicular IVDF appears to be describable as two Maxwellian components (one at a few km/s and one at rest) or a single fast population with a long tail stretching back to zero velocity. Upstream, towards the plasma source (at $z = 165.0$ cm), the perpendicular distribution is slightly narrower than at $z = 167.8$ cm. Therefore, the ion temperature anisotropy increases in the expanding plasma plume.

Moments of the IVDFs are calculated by first performing a Gaussian fit to the IVDF to determine a maximum velocity range to include in a subsequent numerical integration of the measured IVDF (because of the noise inherent in an LIF measurement, integrating the measured IVDFs over all measured velocity values leads to large errors in the integrated moments). The measured IVDFs are integrated using a simple trapezoidal algorithm and higher order moments normalized to the zeroth moment.The numerically determined average speed is used for the reference frame of the second moment, i.e., the effective ion temperature. Throughout this work, we use the descriptor "effective ion temperature" to refer to the square root of the mean squared velocity in the frame of the mean velocity of the ions. The probe is scanned in increments of 2 mm in the radial direction and 4 mm in the axial direction over the measurement region. This region was selected for the high spatial resolution study because previous studies (as shown in Fig. 7) identified the edge of the plasma plume as a region of significant broadening of the perpendicular IVDF.[20]

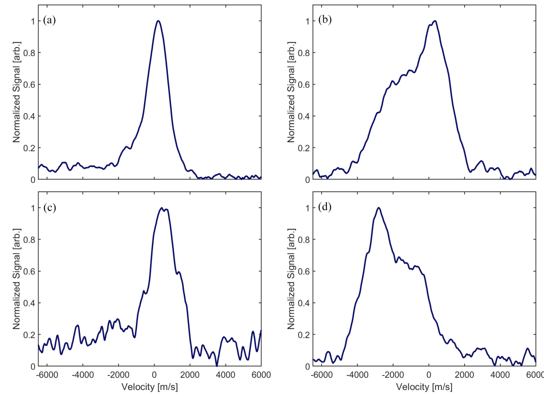

Figure 8. For $z = 167.8$ cm, $r = -5.2$ cm the (a) parallel and (b) perpendicular measurements of the IVDF. For $z = 165.0$ cm, $r = -7.8$ cm the (c) parallel and (d) perpendicular measurements of the IVDF.

Shown in Fig. 9 is a vector field map generated from the first moment ($< v > = \int_{-\infty}^{\infty} v f(v) dv$) in each measurement direction overlaid on a contour plot of the average of the zeroth moments from the perpendicular and parallel measurements ($n \sim \int_{-\infty}^{\infty} f(v) dv$). Note that here the density determined from the LIF-measured IVDFs is the density of the initial ion metastable state and may not fully represent the local ion density as it depends on the local ion and neutral densities, as well as the electron density and electron temperature. The flow vectors were obtained from the first moment of both the perpendicular and parallel measurements. Also shown in Fig. 9 is a representative magnetic field line that shows the direction of the magnetic field in the expansion region.

Unsurprisingly, the metastable ion density decreases as the plasma expands radially and downstream. Previ-

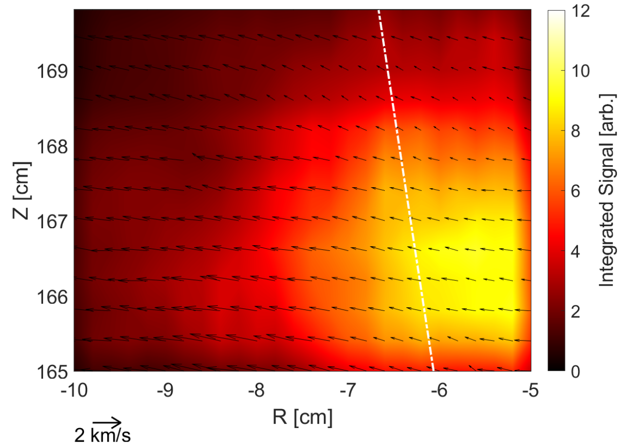

Figure 9. The metastable ion density (zeroth moment of the measured IVDF) in the expanding plasma overlaid with a vector map of the net bulk ion flow obtained from the first moment of both components of the ion flow in the measurement plane. The white line shows the direction of a representative magnetic field line in the expansion region.

ous studies have shown that within a cylindrical region aligned with the system axis, $r < 5$ cm, the ion flow is large, ~ 8 km/s, and entirely axial for these LEIA parameters.[20] At these larger radial locations, the axial bulk ion flow nearly vanishes and weak radial ion flows, $\sim$1 km/s dominate. These bulk flows are also evident in the individual IVDF measurements shown in Fig. 8.

Shown in Fig. 10 for comparison is the time averaged electric field determined from time averaged (over 100 s) measurements of the local plasma potential as measured with the rf-compensated Langmuir probe. Typical potential fluctuations were $\sim 10\%$ of the mean. For some parameters, fluctuation amplitudes up to $\sim 50\%$ were observed. This steady-state electric field arise spontaneously in the plasma and exhibits rapid changes in field direction and magnitude on the scale of 1-2 cm in the outer region of the plasma. The rapid changes in electric field direction follow the expanding magnetic field lines with increasing axial distance from the source and are in the same region where the energetic electrons streaming out from the plasma source are typically observed.[20] Ions and electrons flowing downstream from the plasma source along periphery of the plasma plume will encounter these small (smaller than an ion gyroradius) scale electric field structures. In the high spatial resolution measurement region, the axial electric field is small and generally points towards the source. Therefore, ions in our measurement region will slow down only a modest amount in the axial direction (consistent with the first IVDF measurements) and experience radial electric fields that push ions outward radially and then reverse direction to impart an inward acceleration to the ions in the outer portion of the plume. A critical factor in how the ions respond to such small scale electric field structures is the size of the ion gyroradius. For an argon ion with a perpendicular velocity typical of the effective perpendicular ion temperature obtained from the second moment of the IVDFs in this region, $\sim$ 0.75 eV, the ion gyroradius is 5 cm. Therefore, as soon as an individual ion is energized in the radial direction by these electric fields, the ion will sample the entire measurement region every time it gyrates around the mostly axial magnetic field. In terms of timescales, the gyroperiod is 0.24 ms and the time needed for an argon ion traveling at 1 km/s to travel from one side of the measurement region to the other is only 0.05 ms. In other words, the ions are unmagnetized. The cross-field flow of the ions is ample evidence of demagnetization of the ions. The spatial variation in electric fields over scale of a gyroradius is large enough that guiding center models of the ion motion are not applicable. As discussed below, the effects of these sub-ion gyroradius scale electric field structures on the IVDFs is best understood by looking at the motion of individual ions.

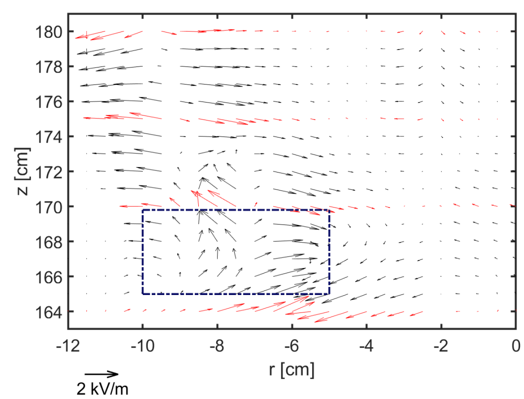

Figure 10. Electric fields measured at discrete axial locations in the expanding plasma plume. The electric field magnitude and direction is determined from gradients of local measurements of the time averaged plasma potential. The dotted box outlines the region for which the high spatial resolution anisotropy measurements were obtained. Actual measurements shown in red, the blue vectors are generated from interpolation between the actual measurements.

Shown in Fig. 11 are the parallel ($\hat{z}$) and perpendicular ($\hat{r}$) ion temperatures calculated from the second moments of the IVDFs. Not only are the parallel ion temperatures much smaller than the perpendicular ion temperatures throughout the measurement region, the axial and radial gradients differ for the two temperature components. Note that these measurements are performed in the laboratory frame. Because the angle between the magnetic field and the experiment axis of symmetry is only 7°, the measured components are, to good approximation, equivalent to parallel and perpendicular components in the frame of the magnetic field. With this caveat, $T_{\perp i}/T_{\parallel i}$ across the measurement region is shown in Fig. 12. The peak in $T_{\perp i}/T_{\parallel i}$ lies along a conical surface that is defined by the expanding magnetic field. The values of $T_{\perp\ i}/T_{\parallel\ i}$ are on the order of 10, a significant level of anisotropy for a laboratory plasma. Given that $\beta_{\parallel\ i}$ is $\sim 10^{-4}$ for these plasmas because of the relatively large magnetic field strengths and the low plasma densities in the expansion region,[20] the plasma conditions are not representative of the solar wind. However, by tuning the downstream magnetic field from 5 - 100 G, it should be possible to explore values of $\beta_{\parallel\ i} \sim 10^{-1}$ to $\sim 10^{-4}$.

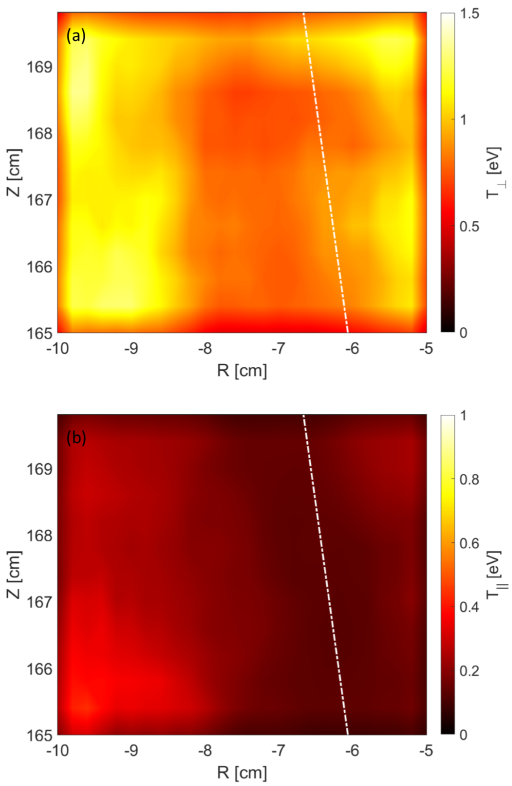

Figure 11. The effective (a) perpendicular ion temperature and (b) parallel ion temperature as a function of radial and axial position. The measurements have been smoothed. The white line indicates the direction of the local magnetic field.

SecondMoment.png

Figure 12. The ion thermal anisotropy as a function of radial and axial position. The measurements have been smoothed. The white line indicates the direction of the local magnetic field.

IV. ANALYSIS

At the plasma densities and ion temperatures typical of the expanding plasma ($n_e \sim 10^{10}$ cm^{-3}, $T_i \sim 1.0$ eV)[26], the ion-ion collisional mean free path is > 1000 cm, greater than the system size. Therefore, collisional thermalization of ion flows is insufficient to explain the observed perpendicular ion heating. Collisional processes, if they were significant, would also quickly equilibrate the perpendicular and parallel ion temperatures. As noted previously, in space, anisotropic particle velocity distributions are believed to excite instabilities which then grow and reduce the anisotropy in a negative feedback process. While it is also possible for instabilities to broaden velocity distributions, the typical assumption is the anisotropy is created by external forces and then relaxes through instability-driven scattering in velocity space. To determine if simple acceleration by the observed small scale electric field structures could be responsible for the large effective perpendicular ion temperatures observed in the expansion region (and therefore be a source for instability excitation), we developed a simple, three-dimensional particle stepper model in cylindrical coordinates using the Boris algorithm, the known magnetic field structure, and the measured electric field structure. The only force on the particles in this model is the Lorentz force. The Boris algorithm[36] advances particle positions based on the Lorentz force and conserves energy exactly in the absence of an electric field. In the presence of an electric field, the error in energy conservation is bounded for all time steps and the error introduces negligible effects on particle motion at later time steps.[37] To model the experiment, we have employed a cylindrical version of the classic Boris algorithm.[38] Ions were advanced in time in steps of $1/(50 f_{ci})$ and electrons were advanced in steps of $1/(3 f_{ce})$, where f_c is the particle's cyclotron frequency calculated using the magnetic field at its current position. The time step is reduced by a factor of 0.15 in the electric field region to capture the dynamics of particles accelerated by the measured electric field. The varying time step is critically important to compensate for possible demagnetization effects in the magnetic field gradient region.

To give the ions a range of parallel and perpendicular velocities as they flowed from the source into the expansion chamber, $100,000$ argon ions were created from a Maxwellian velocity distribution in the parallel direction with a thermal velocity spread corresponding to a temperature of 0.3 eV about a mean parallel flow of 1200 m/s (the thermal velocity corresponding to 0.3 eV). Ions that ended up moving backwards towards the source were eliminated from the simulation. Parallel temperatures of 0.3 eV are typical in the plasma source.[3] To accentuate any perpendicular velocity spreading effects, the initial perpendicular velocity spread was defined by a Maxwellian velocity distribution for a temperature of 0.026 eV, i.e., room temperature. $10,000$ electrons were given thermal spreads in the parallel and perpendicular directions corresponding to temperatures of 3.0 eV.[39] The mean parallel flow speed was set to the thermal speed for 3.0 eV and electrons traveling backwards were also eliminated from the simulation. Ions and electrons were launched from inside the source at $z = 100$ cm and linearly distributed across initial radial positions from $r = 0$ cm to $r = 5$ cm. The measured electric field structure is introduced at $z = 164$ cm. Since the electric field in this region was measured at a radial resolution of 0.5 cm and axial resolution of 5 cm by Aguirre et. al.[20] the measurements were interpolated axially to a resolution of 1 cm. Particles unable to overcome the electric field at that point are reflected upstream and eliminated from the simulation for clarity.

The Boris stepper results are shown in Fig. 13. The most obvious feature is that the electric field structure introduced at $z = 164$ reflects electrons confined to the axis and those at the periphery of the plasma plume back towards the source, creating an annulus of increased electron plasma density surrounding the core. The electron results are consistent with the experimental observations of a hollow population of energetic electrons downstream from the expanding magnetic field.[20]

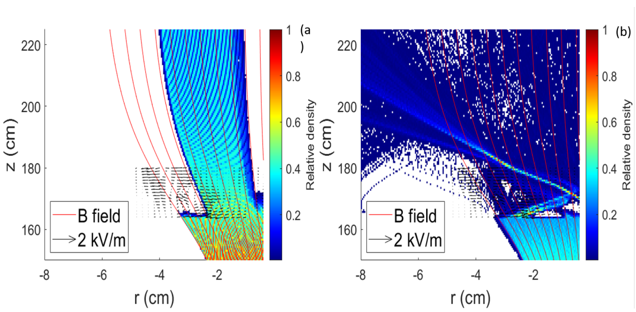

Figure 13. Electrons (a) and argon ions (b) are launched towards the expansion region from inside the plasma source $z = 100$ cm. The particles are advanced with a cylindrical Boris stepper model that incorporates the expanding magnetic field geometry and the measured electric field structures. The particle density maps reveal demagnetization of the ions in the expansion region and magnetized electrons forming an annulus of increased plasma density surrounding the core, consistent with Langmuir probe measurements in LEIA.[20]

The ions, however, behave quite differently. The weakening magnetic field, the highly structured electric field, and the relatively large gyroradius of the ions lead to significant demagnetization of the ions. Individual ions exhibit a wide spread in paths and perpendicular velocities. An example of the induced spread in perpendicular ion velocity is shown Fig. 14a. For comparison, the initial thermally broadened, room temperature ion velocity distribution is shown as a green dotted line in the same figure. The effective perpendicular ion temperature (integrated second moment of the velocity distribution from the model) is shown as a function of radius in Fig. 14b. The qualitative results of the model are striking. There is a significant increase in the spread of the perpendicular IVDF and the increased width increases with increasing radial location - consistent with the measurements. The model results suggest that the observed increase in effective perpendicular ion temperature arises from reversible (non-entropy increasing) motion of ions interacting with a highly structured electric field while simultaneously experiencing a rapid increase in gyroradius.

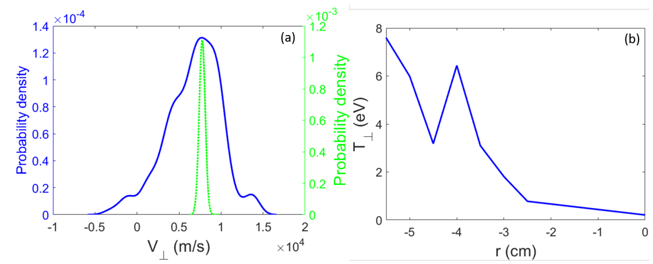

Figure 14. (a) A model-generated IVDF at $z = 167$ cm and $r = -5$ cm is shown in blue. The green dashed line is a Maxwellian IVDF with the same bulk flow as the downstream IVDF from the model and with a width corresponding to 0.026 eV (room temperature). (b) The radial perpendicular temperature profile at $z = 167$ cm.

V. CONCLUSIONS

The highly structured electric field that develops at the periphery of an expanding helicon source plasma consistently generates perpendicular ion velocity space distributions with effective ion thermal anisotropies such that $T_{\perp\, i}/T_{\parallel\, i} \sim 10$. For the scale sizes and time scales of interest, these plasmas are collisionless, i.e. there is no evidence of collisional equilibration between the perpendicular and parallel ion distributions. However, even though $\beta_{\parallel\, i} \sim 10^{-4}$, there is a significant increase in electrostatic wave activity in the plasma when these highly anisotropic ion distributions are created,. Zhang et al., saw strong evidence of wave activity in the ≤ 10 kHz frequency range[35]−the same frequency range that Scime et al. identified as corresponding to electromagnetic AIC waves during the previous laboratory studies of anisotropy driven instabilities.[3] Zhang et al. reported that these intense, near-ion cyclotron frequency waves are localized to the core of the plasma plume and that the wave intensity falls off dramtically outside of the region of large ion thermal anisotropy.[35]

An important issue to consider is if the large thermal anisotropies in these experiments result from a stochastic process, i.e., ion demagnetization in a region of highly structured electric fields, will the resultant velocity distributions be unstable to the same sorts of instabilities that are predicted for solar wind ion populations? In other words, does the plasma care about the origin of wider spread in the perpendicular IVDF compared to the parallel IVDF? An initial exploration of this question was performed by using the measured parallel and perpendicular IVDFs from these experiments as initial conditions for the same computational models that are used to study solar wind ion distributions.[40,41] The model performs a Nyquist stability analysis by modeling the plasma as a collection of relatively drifting bi-Maxwellians.[42] The IVDFs were fit using a Levenberg-Marquardt routine for two Maxwellians and assuming only drifts parallel to the magnetic field. The plasma is best fit using a primary ion population with $\beta_{\parallel\, i,1} = 2.5 \times 10^{-4}$, $w_{\parallel,i,1} = 3.08 \times 10^{-6}c$, $T_{\perp,i,1} = 2.77T_{\parallel,i,1}$ and a secondary ion population with $T_{\parallel,i,2} = 7.65T_{\parallel,i,1}$, $T_{\perp,i,2} = 0.343T_{\parallel,i,2}$, $n_{i,2} = 0.19n_{i,1}$ and a relative drift between the ion populations of $|\Delta v_i| = 0.3v_A$. The electrons are assumed to be $10\times$ hotter than the primary ion population, and quasineutrality and no net current conditions are enforced. The results of the instability analysis are shown in Fig.15. Unstable modes arise at oblique angles to the background magnetic field, with $k_\perp\rho_{i,1} \sim 1$ and $k_{||}\rho_{i,1} \sim 0.2$, for perpendicular scales comparable to the 5 cm gyroradius and for parallel scales roughly five times the gyroradius - both scales consistent with the geometry of the experiment. These fastest growing modes have propagation directions aligned with the drift of the secondary ion component and frequencies comparable to Ω_i, seen in Fig. 15b) where we follow the normal mode dispersion relation for the fastest growing mode along the grey dashed line from panel Fig. 15a. The power absorbed ($\gamma_j < 0$, dashed lines) or emitted ($\gamma_j > 0$, solid) per wave period from each of the three components (red, blue, and green are the primary ion, secondary ion, and electron populations) is shown in panel c, as well as the total damping or growth rate (black line). We do not find parallel propagating unstable waves of the kind driven by the temperature anisotropy of a single ion distribution. Rather, the oblique instabilities are driven when the power being emitted from the secondary ion population, is greater than that absorbed by the primary ion population and the electrons combined. This is similar to the kinds of oblique ion beam instabilities predicted to arise in the solar wind,[43] and possibly observed *in situ* by Parker Solar Probe.[44] Importantly, these instability analysis results do not depend on how the IVDFs are created, but rather on the details of the parallel and perpendicular velocity distributions at the measured spatial location, which provide free energy for the growth of unstable waves.

VI. ACKNOWLEDGEMENTS

We thank Prof. Paul Cassak of West Virginia University for helpful discussions. This work was supported by U.S. National Science Foundation Grant No. PHY-1902111 and Department of Energy Grant DE-SC0020294. KGK was supported by NASA Grant 80NSSC19K0912.

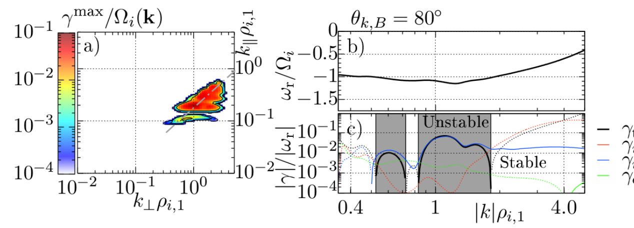

Figure 15. Nyquist stability analysis based on the parallel and perpendicular IVDF measurements in the experiment. (a) unstable modes appear for for $k\rho_{i,1} \sim 1$ and $\theta_{k,B} \sim 80°$ (grey dashed line). (b) The fastest growing unstable modes propagate in the same direction as the secondary ion population. (c) The unstable wavevectors, solid black lines, are driven by power being emitted by the secondary ion population (blue lines) while both the primary ion (red) and electron (green) populations act to absorb some of the emitted power.

DATA AVAILABILITY

The data that support the findings of this study are available from the corresponding author upon reasonable request.

REFERENCES

[1] L. Matteini, P. Hellinger, S. Landi, P. Trávníček, and M. Velli, "Ion kinetics in the solar wind: Coupling global expansion to local microphysics," Space Science Reviews **172**, 373–396 (2012).
[2] J. C. Kasper, A. J. Lazarus, S. P. Gary, and A. Szabo, "Solar wind temperature anisotropies," AIP Conference Proceedings **679**, 538–541 (2003).
[3] E. Scime, P. A. Keiter, S. P. Gary, M. M. Balkey, R. F. Boivin, J. L. Kline, and M. Blackburn, "Ion temperature anisotropy limitation in high beta plasmas," Physics of Plasmas **7**, 2157–2165 (2000).
[4] S. D. Bale, J. C. Kasper, G. G. Howes, E. Quataert, C.Salem, and D. Sundkvist, "Magnetic fluctuation power near proton temperature anisotropy instability thresholds in the solar wind," Phys. Rev. Lett. **103**, 211101 (2009).
[5] C. H. K. Chen, L. Matteini, A. A. Schekochihin, M. L. Stevens, C. S. Salem, B. A. Maruca, M. W. Kunz, and S. D. Bale, "Multi-species Measurements of the Firehose and Mirror Instability Thresholds in the Solar Wind," Astrophys. J. Lett. **825**, L26 (2016), arXiv:1606.02624 [physics.space-ph].
[6] D. Verscharen, K. G. Klein, and B. A. Maruca, "The multi-scale nature of the solar wind," Living Rev. Solar Phys. **16**, 5 (2019), arXiv:1902.03448 [physics.space-ph].
[7] S. P. Gary, *Theory of Space Plasma Microinstabilities* (Cambridge University Press, 1993).
[8] S. P. Gary, J. Wang, D. Winske, and S. A. Fuselier, "Proton temperature anisotropy upper bound," Journal of Geophysical Research: Space Physics **102**, 27159–27169 (1997).
[9] P. Hellinger, P. Trávníček, J. C. Kasper, and A. J. Lazarus, "Solar wind proton temperature anisotropy: Linear theory and wind/swe observations," Geophysical Research Letters **33**, L09101 (2006).
[10] S. R. Cranmer, Astrophys. J. Suppl. Ser. **213**, 16 (2014).
[11] N. Ozak, L. Ofman, and A.-F. Viñas, The Astrophysical Journal **799**, 77 (2015).

[12]P. H. Yoon, J. Seough, C. S. Salem, and K. G. Klein, "Solar wind temperature isotropy," Phys. Rev. Lett. **123**, 145101 (2019).
[13]D. Verscharen, B. D. G. Chandran, K. G. Klein, and E. Quataert, "Collisionless Isotropization of the Solar-wind Protons by Compressive Fluctuations and Plasma Instabilities," Astrophys. J. **831**, 128 (2016), arXiv:1605.07143 [physics.space-ph].
[14]B. Anderson, R. Denton, G. Ho, D. Hamilton, S. Fuselier, and R. Strangeway, "Observational test of local proton cyclotron instability in the earth's magnetosphere," Advanced Earth and Space Science **101**, 21527–21543 (1996).
[15]C. F. Kennel and H. Petschek, "Limit on stably trapped particle fluxes," Journal of Geophysical Research (1896-1977) **71**, 1–28 (1966).
[16]R. C. Davidson and J. M. Ogden, "Electromagnetic ion cyclotron instability driven by ion energy anisotropy in highbeta plasmas," The Physics of Fluids **18**, 1045–1050 (1975).
[17]G. R. Smith, "Alfvn ioncyclotron instability in tandemmirror plasmas. i," The Physics of Fluids **27**, 1499–1513 (1984).
[18]B. A. Maruca, A. Chasapis, S. P. Gary, R. Band yopadhyay, R. Chhiber, T. N. Parashar, W. H. Matthaeus, M. A. Shay, J. L. Burch, T. E. Moore, C. J. Pollock, B. J. Giles, W. R. Paterson, J. Dorelli, D. J. Gershman, R. B. Torbert, C. T. Russell, and R. J. Strangeway, "MMS Observations of Beta-dependent Constraints on Ion Temperature Anisotropy in Earth's Magnetosheath," Astrophys. J. **866**, 25 (2018), arXiv:1806.08886 [physics.space-ph].
[19]P. A. Keiter, E. E. Scime, M. M. Balkey, R. Boivin, J. L. Kline, and S. P. Gary, "Beta-dependent upper bound on ion temperature anisotropy in a laboratory plasma," Physics of Plasmas **7**, 779–783 (2000).
[20]E. Aguirre, E. Scime, D. Thompson, and T. Good, "Spatial structure of ion beams in an expanding plasma," Physic of Plasmas **24**, 123510 (2017).
[21]A. M. Keesee and E. E. Scime, "Neutral density profiles in argon helicon plasmas," Plasma Sources Science and Technology **16**, 742–749 (2007).
[22]D. S. Thompson, T. E. Steinberger, A. M. Keesee, and E. E. Scime, "Laser Induced Fluorescence of Ar-I Metastables in the Presence of a Magnetic Field," **27**, 065007 (2018), plasma Sources Sci. Technol.
[23]E. E. Scime, P. A. Keiter, M. M. Balkey, J. L. Kline, X. Sun, A. M. Keesee, R. A. Hardin, I. A. Biloiu, S. Houshmandyar, S. C. Thakur, J. J. Carr, M. Galante, D. McCarren, and S. Sears, "The hot helicon experiment (helix) and the large experiment on instabilities and anisotropy (leia)," J. Plasma Physics **81**, 345810103 (2014).
[24]J. Carr, *Laser Induced Fluorescence Studies of Electrostatic Double Layers in an Expanding Helicon Plasmas*, Ph.D. thesis, West Virginia University (2013).
[25]R. F. Boivin, "Zeeman splitting for lif transitions and deconvolution technique to extract ion temperature," Tech. Rep. PAPS-E-PHPAEN-10-003306 (West Virginia University, 2003).
[26]E. Aguirre, *Spontaneous Formation of Ion Holes and Ion Beams in Expanding Plasmas*, Ph.D. thesis, West Virginia University (2018).
[27]C. Charles and R. Boswell, "Current-free double-layer formation in a high-density helicon discharge," Applied Physics Letters **82**, 13561358 (2003).
[28]S. A. Cohen, N. S. Seifert, S. Stange, E. E. Scime, R. F. Boivin, and F. Levinton, "Ion acceleration in plasmas emerging from a helicon-heated magnetic-mirror device," Physics of Plasmas **10**, 2593–2598 (2003).
[29]X. Sun, C. Biloiu, R. Hardin, and E. E. Scime, "Parallel velocity and temperature of argon ions in an expanding, helicon source driven plasma," Plasma Sources Science and Technology **13**, 359–370 (2004).
[30]D. Thompson, I. Furno, A. Howling, R. Jacquier, G. Plyushchey, and E. E. Scime, "Ion heating and flows in a high power helicon source," Phys. Plasmas **24**, 063517 (2017).
[31]Y. T. Sung, Y. Li, and J. E. Scharer, "Fast, hot electron production and ion acceleration in a helicon inductive plasma," Physics of Plasmas **23**, 092113 (2016).
[32]A. Bennet, C. Charles, and R. Boswell, "In situ electrostatic characterisation of ion beams in the region of ion acceleration," Physics of Plasmas **25**, 023516 (2018).
[33]A. Bennet, C. Charles, and R. Boswell, "Selective radial release of hot, magnetised electrons downstream of a low-pressure expanding plasma," Journal of Physics D: Applied Physics **51**, 375204 (2018).
[34]A. Bennet, C. Charles, and R. Boswell, "Non-local plasma generation in a magnetic nozzle," Physics of Plasmas **26**, 072107 (2019).
[35]Y. Zhang, C. Charles, and R. Boswell, "Effect of radial plasma transport at the magnetic throat on axial ion beam formation," Physics of Plasmas **23**, 083515 (2016).
[36]C. K. Birdsall, "Particle-in-cell charged-particle simulations, plus monte carlo collisions with neutral atoms, pic-mcc," IEEE Transactions on Plasma Science **19**, 65–85 (1991).
[37]H. Qin, S. Zhang, J. Xiao, J. Liu, Y. Sun, and W. M. Tang, "Why is boris algorithm so good?" Physics of Plasmas **20**, 084503 (2013).
[38]G. Delzanno and E. Camporeale, "On particle movers in cylindrical geometry for particle-in-cell simulations," Journal of Computational Physics **253**, 259 – 277 (2013).
[39]D. Thompson, S. Keniley, M. Henriquez, D. Correlli, M. U. Siddiqui, and E. E. Scime, "Three-dimensional cross-field flows at the plasma-material interface in an oblique magnetic field," Physics of Plasmas **27**, 073511 (2020).
[40]K. G. Klein, B. L. Alterman, M. L. Stevens, D. Vech, and J. C. Kasper, "Majority of Solar Wind Intervals Support Ion-Driven Instabilities," Phys. Rev. Lett. **120**, 205102 (2018), arXiv:1804.06330 [physics.space-ph].
[41]K. G. Klein, M. Martinović, D. Stansby, and T. S. Horbury, "Linear Stability in the Inner Heliosphere: Helios Re-evaluated," Astrophys. J. **887**, 234 (2019), arXiv:1912.00250 [astro-ph.SR].
[42]K. G. Klein, J. C. Kasper, K. E. Korreck, and M. L. Stevens, "Applying nyquist's method for stability determination to solar wind observations," Journal of Geophysical Research (Space Physics) **122**, 9815–9823 (2017).
[43]D. Verscharen and B. D. G. Chandran, "The Dispersion Relations and Instability Thresholds of Oblique Plasma Modes in the Presence of an Ion Beam," Astrophys. J. **764**, 88 (2013), arXiv:1212.5192 [physics.space-ph].
[44]J. L. Verniero, D. E. Larson, R. Livi, A. Rahmati, M. D. McManus, P. S. Pyakurel, K. G. Klein, T. A. Bowen, J. W. Bonnell, B. L. Alterman, P. L. Whittlesey, D. M. Malaspina, S. D. Bale, J. C. Kasper, A. W. Case, K. Goetz, P. R. Harvey, K. E. Korreck, R. J. MacDowall, M. Pulupa, M. L. Stevens, and T. D. de Wit, "Parker Solar Probe Observations of Proton Beams Simultaneous with Ion-scale Waves," Astrophys. J. Supp. **248**, 5 (2020), arXiv:2004.03009 [physics.space-ph].
[45]B. S.D., J. Kasper, G. Howes, E. Quataert, C. Salem, and D. Sundkvist, "Magnetic fluctuation power near proton temperature anisotropy instability thresholds in the solar wind," Physical Review Letters **103**, 4 (2009).
[46]S. Gary, M. Montgomery, W. Feldman, and D. Forslund, "Proton temperature anisotropy instabilities in the solar wind," Journal of Geophysical Research **81**, 6 (1976).
[47]S. Stverak, P. Travnicek, M. Maksimovic, A. N. Marsch, Fazakerley, and E. E. Scime, "Electron temperature anisotropy constraints in the solar wind," Journal of Geophysical Research **113**, 10 (2008).
[48]S. Peter Gary, H. Li, S. O'Rourke, and D. Winske, "Proton resonant firehose instability: Temperature anisotropy and fluctuating field constraints," Journal of Geophysics Research **103**, 8 (1998).

[49]N. Singh, "Current-free double layer: A review," Physics of Plasmas **18**, 122105 (2011).
[50]M. Leubner and N. Schupfe, "Mirror instability thresholds in suprathermal space plasmas," Journal of Geophysical Research **105** (2000), 10.1029/1999JA000447.
[51]A. Hasegawa, "Drift mirror instability in the magnetoshpere," The Physics of Fluids **12**, 10 (1969).
[52]M. Lazar and S. Poedts, "Limits for the firehose instability in space plasmas," Solar Physics **258**, 119–128 (2009).
[53]A. M. E. E. S. Keesee, C. Charles, A. Meige, and R. Boswell, "The ion velocity distribution function in a current-free double layer," Phys. Plasma **12**, 093502 (2005).